Monthly Notices
of the
ROYAL ASTRONOMICAL SOCIETY

MNRAS **514,** 4413–4425 (2022)
Advance Access publication 2022 June 15

https://doi.org/10.1093/mnras/stac1634

ExoMol photodissociation cross-sections – I. HCl and HF

Marco Pezzella, Jonathan Tennyson ★ and Sergei N. Yurchenko

Department of Physics & Astronomy, University College London, London WC1E 6BT, UK

Accepted 2022 June 9. Received 2022 June 9; in original form 2022 February 5

ABSTRACT

Photon initiated chemistry, i.e. the interaction of light with chemical species, is a key factor in the evolution of the atmosphere of exoplanets. For planets orbiting stars in UV-rich environments, photodissociation induced by high-energy photons dominates the atmosphere composition and dynamics. The rate of photodissociation can be highly dependent on atmospheric temperature, as increased temperature leads to increased population of vibrational excited states and the consequent lowering of the photodissociation threshold. This paper inaugurates a new series of papers presenting computed temperature-dependent photodissociation cross-sections with rates generated for different stellar fields. Cross-sections calculations are performed by solving the time-independent Schrödinger equation for each electronic state involved in the process. Here, photodissociation cross-sections for hydrogen chloride and hydrogen fluoride are computed for a grid of 34 temperatures between 0 and 10 000 K. Use of different radiation fields shows that for the Sun and cooler stars the photodissociation rate can increase exponentially for molecular temperatures above 1000 K; conversely the photodissociation rates in UV rich fields instead are almost insensitive to the temperature of the molecule. Furthermore, these rates show extreme sensitivity to the radiation model used for cool stars, suggesting that further work on these may be required. The provision of an ExoMol data base of cross-sections is discussed.

Key words: molecular data – radiative transfer – planets and satellites: atmospheres.

1 INTRODUCTION

The interaction of photons with molecules, known as photochemistry, plays an important role in the atmospheric composition and dynamics of planets and exoplanets. It is especially important for all the exoplanets that orbit near their host star, as those planets experience strong UV-rich stellar fields (Madhusudhan et al. 2016; Venot et al. 2016; Badhan et al. 2019; Fleury et al. 2019; Lewis et al. 2020; Teal et al. 2022). Measurements of photodissociation cross-sections have been performed mostly at low temperatures, but, even when high-temperature measurements are available (Venot et al. 2016), they struggle to reach temperatures of interest for planetary atmospheres ($T > 1000$ K). The existing models and data bases (Heays, Bosman & van Dishoeck 2017; Noelle et al. 2020) are only adequate for cold molecules in the interstellar medium, where molecules are in their vibrational ground states (Valiev et al. 2020). There is a long history of theoretical photodissociation studies (Schinke 1993), but only recently was the importance of the temperature effects demonstrated (Grebenshchikov 2016). Those effects are important for modelling non-local thermodynamic effects (non-LTE), with the photodissociation being one of the major driving forces of the non-LTE effects (Clark & Yurchenko 2021), along with radiative, (photo-)chemical, energy transfer, and other processes (López-Puertas & Taylor 2001).

The ExoMol data base (Tennyson et al. 2016, 2020) was designed to produce comprehensive line lists of hot bound–bound transitions for molecules that are important in exoplanet atmospheres (Tennyson & Yurchenko 2012; Tennyson et al. 2020). In our previous work (Pezzella, Yurchenko & Tennyson 2021) we showed how the programs DUO (Yurchenko et al. 2016), originally developed to solve the bound–bound nuclear motion problem for diatomics using a grid-based variational solution of the Schrödinger equation including different types of couplings and crossings, and EXOCROSS (Yurchenko, Al-Refaie & Tennyson 2018) can be used to produce photodissociation cross-sections by averaging the results of DUO calculations obtained using different radial grids and smoothing the results with an appropriate Gaussian function. With this work we start a new branch of the ExoMol project that aims to provide temperature-dependent photodissociation data (cross-sections and rates) for molecules found in exoplanetary atmospheres and elsewhere. The first two molecules studied are HCl and HF. The $A\,^1\Pi \leftarrow X\,^1\Sigma^+$ photodissociation transitions of these molecules formed part of the test cases used to shape our methodology (Pezzella et al. 2021); here we extend our model to more states covering both direct and indirect photodissociations and consider the effects of temperature on the molecules.

Chlorine has a relative abundance with respect to hydrogen of 3×10^{-7} (Asplund et al. 2009); it has two stable isotopologues (^{35}Cl, ^{37}Cl), with a terrestrial isotope ratio close to 3:1. HCl is the only chlorine-bearing molecule observed in the interstellar media. The molecule has been detected in the circumstellar envelope of the carbon-rich star IRC + 10216, with a molecular abundance with respect to H_2 of 6×10^{-7} (Cernicharo et al. 2010), in molecular clouds as OMC-1 (Blake, Keene & Phillips 1985; Schilke, Phillips & Wang 1995), Sagittarius B2 (Zmuidzinas et al. 1995), ρ Ophiuci

★ E-mail: j.tennyson@ucl.ac.uk

(Federman et al. 1995), and W31C (Monje et al. 2013). HCl has been used by Maas & Pilachowski (2018) for determining the isotope ratio $^{35}Cl/^{37}Cl$ in six M giant stars, finding an average value of $\frac{^{35}Cl}{^{37}Cl} = 2.66 \pm 0.58$. The molecule is expected to be found in low quantities on Jupiter's atmosphere (Teanby et al. 2014). There is only one stable isotope of fluorine with an abundance relative to hydrogen of 3.6×10^{-8} (Asplund et al. 2009). Hydrogen fluoride has been identified by Neufeld et al. (1997) in the interstellar medium (for example in the W31C (Neufeld et al. 2010), W49N, and W51 (Sonnentrucker et al. 2010)) and in cool stellar atmospheres of AGB stars by Uttenthaler et al. (2008), and later was identified in two nearby galaxies (NGC 253 and NGC 4945) with an estimated abundance with respect to H_2 of 6×10^{-9} (Monje et al. 2014). Developments in the observations of HCl and HF, and their application in modelling approaches are found in Gerin, Neufeld & Goicoechea (2016).

The paper is structured as follows: the method section describes the methodology used for computing the photodissociation cross-sections and rates, giving the sources of our potential energy curves and transition dipole moments. The following two sections present our results and Section 5 briefly outlines the upcoming data base. Finally, Section 6 gives our conclusions.

2 METHODS

2.1 Potential energy and transition dipole moment curves

Although the ExoMol data base provides line lists for both HCl and HF, these were actually taken from the work of Li et al. (2013a, b), as incorporated in HITRAN (Gordon et al. 2017), which provides pure-rotational and ro-vibrational transition data over an extended temperature energy range. This means we had to build spectroscopic models for the rovibronic transitions from scratch for the current study.

We consider 9 electronic states of HCl, whose minima lie below the H ionization limit at approximately 100 000 cm^{-1}, see Fig. 1. Potential energy curves (PECs) of the $X\,^1\Sigma^+$ and $A\,^1\Pi$ states are taken from Alexander, Pouilly & Duhoo (1993), the transition dipole moment curve (TDMC) between those states is from Givertz & Balint-Kurti (1986). In this case, the choice of using this combination of a PEC and a TDMC from two different sources has been validated by the comparison of our results with the experiments from different sources (Pezzella et al. 2021). All other PECs and TDMCs are taken from Engin, Sisourat & Carniato (2012). The potentials are described using the cubic spline interpolation implemented in DUO. The $A\,^1\Pi$ potential is a repulsive state that asymptotically goes to the ground state $H(^2S) + Cl(^2P)$ dissociation limit. The $B\,^1\Sigma^+$ state has a double well structure with the lowest minimum near 2.44 Å (at 71948.2 cm^{-1}), and a second minimum near 1.35 Å (at 76643.3 cm^{-1}); the two minima are separated by a barrier of 4695 cm^{-1}. The double well structure of the $B\,^1\Sigma$ state arises from the avoided crossing between two states, identified as $E\,^1\Sigma^+$ and $V\,^1\Sigma^+$, however, for the photodissociation process there is no advantage in treating the two states separately (Lefebvre-Brion, Liebermann & Vázquez 2011). The potential energy curves from Engin et al. (2012) were shifted to improve the agreement with the experimental results from Cheng et al. (2002) and Li et al. (2006) for the $C\,^1\Pi$, $D\,^1\Pi$, $H\,^1\Sigma^+$, $K\,^1\Pi$, $M\,^1\Pi$ states; the $B\,^1\Sigma^+$, $5\,^1\Pi$, and $4\,^1\Sigma^+$ are shifted in order to keep constant the energy differences with the surrounding states. The TDMCs are described by interpolation.

We neglect the coupling contributions from the $a\,^3\Pi \leftarrow X\,^1\Sigma^+$, the $b\,^3\Pi \leftarrow X\,^1\Sigma^+$, and the $t\,^3\Sigma \leftarrow X\,^1\Sigma^+$ bands, as their contributions

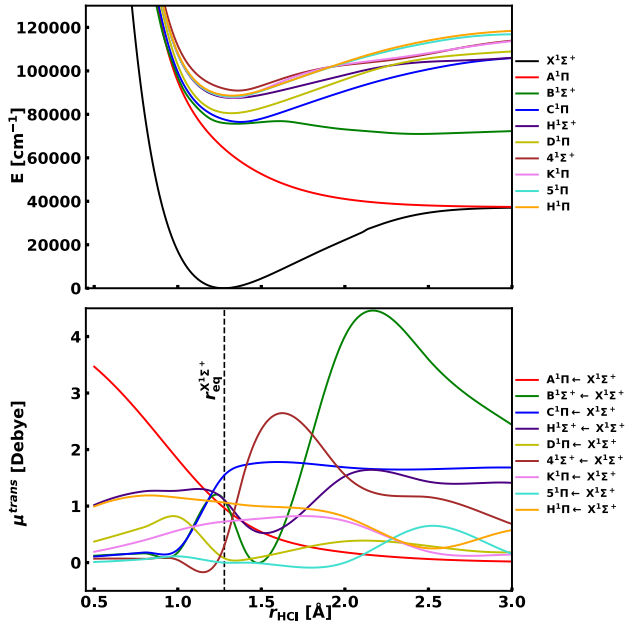

Figure 1. Potential energy curves and transition dipole moments of HCl. PECs of the $X\,^1\Sigma^+$ and $A\,^1\Pi$ states are taken from Alexander et al. (1993), TDMC of $A\,^1\Pi \leftarrow X\,^1\Sigma^+$ is from Givertz & Balint-Kurti (1986). The other PECs and TDMCs are taken from Engin et al. (2012).

to the wavefunction are less than 1 per cent (Engin et al. 2012). The $b\,^3\Pi \leftarrow X\,^1\Sigma^+$ band contribution to the photodissociation rates is estimated to be 1.0×10^{-11} s^{-1}, less than the 1 per cent of the total photodissociation rate. Tilford, Ginter & Vanderslice (1970) observed that the $b\,^3\Pi \leftarrow X\,^1\Sigma^+$ cross-sections are 40–50 times weaker than the $C\,^1\Pi \leftarrow X\,^1\Sigma^+$ ones. Zhang (2008) showed that dissociation from the $t\,^3\Sigma^+$ state occurs through the spin–orbit coupling with the $A\,^1\Pi$ state.

For HF we consider four electronic states: $X\,^1\Sigma^+$, $A\,^1\Pi$, $B\,^1\Sigma^+$, and $C\,^1\Pi$, see Fig. 2. The PECs of the $X\,^1\Sigma^+$, $B\,^1\Sigma^+$, and $C\,^1\Pi$ states and the transition moments involved are taken from Liu et al. (2021), the $A\,^1\Pi$ PEC and the $A\,^1\Pi \leftarrow X\,^1\Sigma^+$ TDMC are from Brown & Balint-Kurti (2000). We use Morse potentials to describe the $X\,^1\Sigma^+$ and $C\,^1\Pi$ PECs. The $A\,^1\Pi$, $B\,^1\Sigma^+$ PECs, and corresponding TDMCs are described using DUO's cubic spline interpolations. The $A\,^1\Pi$ – $X\,^1\Sigma^+$ band is the only electronic band below 100 000 cm^{-1}, as the $B\,^1\Sigma^+$ and $C\,^1\Pi$ states lie above the H_2 ionization threshold.

The assumption that coupling between different electronic states can be neglected without significantly affecting the overall photodissociation cross-section process means that separate DUO calculations can be performed for each excited state. DUO input files for each single electronic excitation are given in the electronic supplementary material: a total of 9 files for HCl and 3 for HF. If one wishes to consider curve couplings, then multiple electronic states can be considered within the same DUO input structures.

2.2 Cross-sections calculations

In this section, we briefly describe how the photodissociation cross-sections are computed with a detailed description given by Pezzella et al. (2021). Our method is based on solving the time-independent Schrödinger equation using DUO (Yurchenko et al. 2016) and then post-processing the discretized results using EXOCROSS (Yurchenko et al. 2018) to give continuous, smooth cross-sections. Our previous numerical experiments showed that use of discretized and smoothed

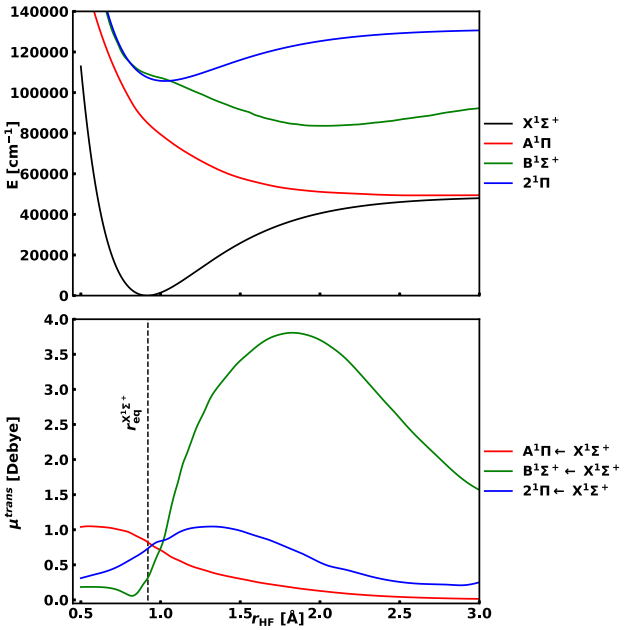

Figure 2. Potential energy and transition dipole moment curves of HF. PECs of the $X\,^1\Sigma^+$, $B\,^1\Sigma^+$, and $C\,^1\Pi$ states, and the involved transition dipole moments are taken from Liu et al. (2021). PEC of the $A\,^1\Pi$ state and the $A\,^1\Pi \leftarrow X\,^1\Sigma^+$ TDMC are from Brown & Balint-Kurti (2000).

Table 1. Temperatures (T) at which the cross-sections and rates presented in this work are calculated.

T (K)				
0	100	200	300	400
500	600	700	800	900
1000	1100	1200	1300	1400
1500	1600	1700	1800	1900
2000	2200	2400	2600	2800
3000	3200	3400	3600	4000
4500	5000	5500	10000	

results led to the same photodissociation rates with respect to previously published cross-sections (van Dishoeck, van Hemert & Dalgarno 1982; Brown & Balint-Kurti 2000; Cheng et al. 2002) when considered with an appropriate (stellar) radiation field; here rates are generated using the smoothed cross-sections.

The photodissociation cross-sections for each electronic states are evaluated for 34 temperatures between $T = 0$ and $T = 10\,000$ K. Here, T is excitation temperature of the gas describing the state population of via the Boltzmann law and assuming the local-thermal-equilibrium (LTE) and the temperature of the radiation field. The total cross-section is obtained summing together the partial contributions. Table 1 reports the individual temperatures. We assume that every excitation to an electronic state above the dissociation limits leads to a dissociative event. The same assumption is made by the Leiden data base (Heays et al. 2017).

At a given temperature T, the photodissociation cross-section of a single electronic transition is calculated by averaging 100 individual cross-sections produced by varying the radial grid size representing the range of the nuclear bond distances r. For each radial grid size r_{max}, the Schrödinger equation for the system is solved, where the unbound states are treated as a particle in box problem, on the basis of 'bound' vibrational functions that vanish exactly at $r = r_{max}$, as part

Table 2. HF and HCl isotopologues studied in this work.

Molecule	Mass (Dalton)	Nuclear spin
HF	20.01	$\frac{1}{2}, \frac{1}{2}$
DF	21.01	$1, \frac{1}{2}$
$H^{35}Cl$	35.98	$\frac{1}{2}, \frac{3}{2}$
$D^{35}Cl$	36.98	$1, \frac{3}{2}$
$H^{37}Cl$	37.97	$\frac{1}{2}, \frac{3}{2}$
$D^{37}Cl$	38.98	$1, \frac{3}{2}$

of the Sinc DVR approach (Colbert & Miller 1992). The resulting eigenvalues and eigenfunctions are then used to obtain temperature-dependent cross-sections corresponding to the electronic, bound–bound, and bound–free transitions. The bound–bound transitions are unaffected by a change in the radial grid, while the bound–free transitions are sensitive to the increase grid size, as it increases the number of discrete 'particle-in-the-box' states included in the Duo calculation. The single cross-sections corresponding to different grid sizes are averaged and smoothed using a normalized Gaussian smoothing function. The Schrödinger equation is solved between $r_{min} = 0.5$ Å and $r_{max} = 3.0$–3.1 Å with an increase of 0.001 Å, using a Sinc DVR basis set. In the Sinc DVR method, the interatomic distance is represented by a uniformly spaced grid points distributed between r_{min} and r_{max}; the Schrödinger equation is transformed to an eigenmatrix problem. The real symmetric Hamiltonian matrix is then diagonalized for each J (total angular momentum) and parity. Energies up to hc 150 000 cm^{-1}, $J_{max} = 120$ and vibrational levels up to $v = 200$ are considered. For each grid size, a line list (energies and Einstein A coefficients) is produced with the thresholds of 10^{-30} cm molecule^{-1} set for line intensities at $T = 10\,000$ K and of 10^{-30} D^2 for line strengths. Each line list is then used to calculate temperature-dependent absorption coefficients (cm/molecule), binned into a wavenumber grid with the typical spacing of 4 cm^{-1}. Each binned spectrum for a given T represents absorption transitions to a selection of unbound states corresponding to a given grid of r_{max}. Different spectra are then averaged and smoothed with an appropriate Gaussian profile to produce the final absorption cross-section (cm^2/molecule) for each temperature T. A Gaussian smoothing function is used with its width varying depending on the nature of the electronic transition. A half-width of half-maximum (HWHM) of 12.5 cm^{-1} was used for all bound–bound transitions ($C\,^1\Pi \leftarrow X\,^1\Sigma^+$ for both molecules, $D\,^1\Pi \leftarrow X\,^1\Sigma^+$, $H\,^1\Pi \leftarrow X\,^1\Sigma^+$, $M\,^1\Pi \leftarrow X\,^1\Sigma^+$, $4\,^1\Sigma^+ \leftarrow X\,^1\Sigma^+$, and the $5\,^1\Pi \leftarrow X\,^1\Sigma^+$ for HCl only) to reproduce the experimental cross-sections by Nee, Suto & Lee (1985), Cheng et al. (2002), and Li et al. (2006) for HCl and Hitchcock et al. (1984) for HF. The bound to dissociative $A\,^1\Pi \leftarrow X\,^1\Sigma$ transitions of HCl and HF are smoothed using a Gaussian function with width a of 50 and 45 cm^{-1}, respectively. A width of 125 cm^{-1} is used to describe the $B\,^1\Sigma \leftarrow X\,^1\Sigma$ bound–bound transitions. The necessity of a large width for this transition derives from the fact that the $B\,^1\Sigma^+$ state is characterized by a small vibrational intervals and rotational constants (Tilford & Ginter 1971).

Calculations are performed on both hydrogen and deuterium isotopologues of HCl and HF, and ^{35}Cl and ^{37}Cl isotopes for HCl. Isotopologue data are presented in Table 2. Each isotopologue cross-section is presented for 100 per cent abundance.

2.3 Radiation field and interstellar rates

Photodissociation rates can be used as an alternative to the cross-sections; they are used for modelling the abundance and temporal

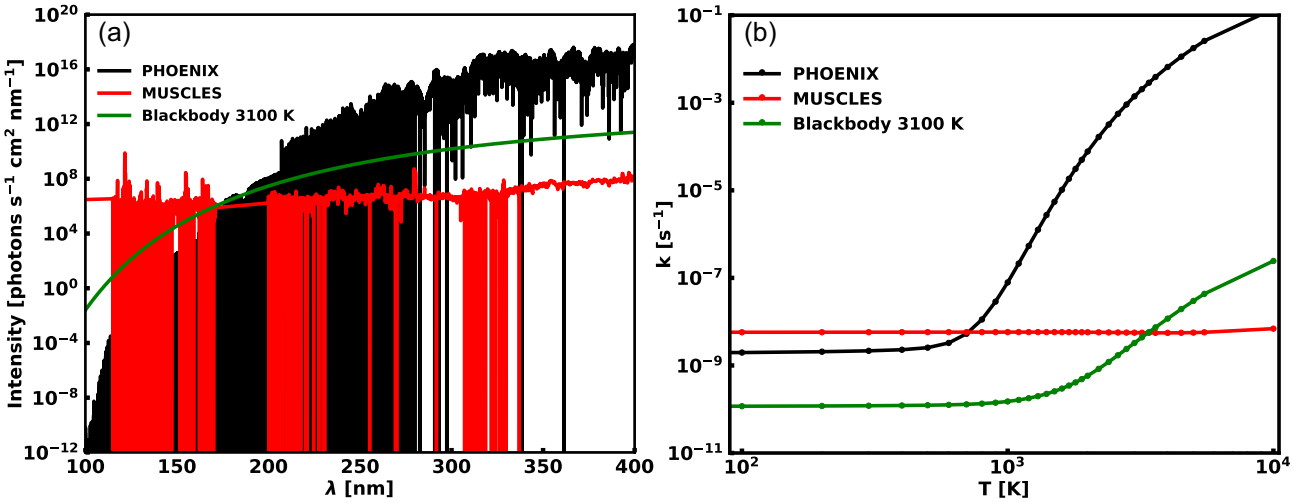

Figure 3. Panel A: different radiation fields models used for describing Proxima Centauri. The PHOENIX model (Husser et al. 2013) is in black, MUSCLES model (Youngblood et al. 2017) in red, and the black-body in green. Panel B: HCl photodissociation rates between 100 and 10 000 K using the different Proxima Centauri stellar fields.

evolution of chemical species in the interstellar medium or in stellar and planetary atmospheres (Wakelam et al. 2012, 2015).

The temperature-dependent photodissociation rate $k(T)$ of a molecule dissociated by a field with a flux $F(\lambda)$ between the wavelengths λ_1 and λ_2 is expressed as

$$k(T) = \int_{\lambda_1}^{\lambda_2} F(\lambda)\sigma(\lambda, T)\mathrm{d}\lambda. \quad (1)$$

Here and elsewhere T refers to the temperature of the internal states of the molecule under consideration.

There are several standard fluxes used to produce appropriate rates, depending on which region of space is observed. The interstellar radiation field (ISRF) has been fitted by Draine (1978) to an analytical expression for wavelengths between 91.2 nm and 200 nm and was expressed as

$$F(\lambda) = 3.2028 \times 10^{13}\lambda^{-3} - 5.1542 \times 10^{15}\lambda^{-4} + 2.0546 \times 10^{17}\lambda^{-5}, \quad (2)$$

where λ is the wavelength in nm, and it was later extended to 2000 nm by van Dishoeck & Black (1982) using the expression:

$$F(\lambda) = 3.67 \times 10^{4}\lambda^{0.7}. \quad (3)$$

The stellar field is expressed in units of photons s^{-1} cm^{-2} nm^{-1}.

The black-body radiation field, $B(\lambda, T_{\rm rad})$, is used as an approximation of a generic stellar field at a temperature $T_{\rm rad}$, and expressed in units of photons s^{-1} cm^{-2} nm^{-1}. The general expression for this field is

$$B(\lambda, T_{\rm rad}) = \frac{2 \times 10^4}{4\pi\lambda^4} \frac{1}{e^{\frac{hc}{\lambda k_{\rm B} T_{\rm rad}}} - 1} \quad (4)$$

$h = 6.626 \times 10^{-34}$ J $\times$s is the Planck constant, c is the speed of light, and $k_{\rm B} = 1.381 \times 10^{-23}$ J K^{-1} is the Boltzmann constant. We consider several different temperatures, describing different types of stars, in a similar fashion to the work performed by Heays et al. (2017). The temperature $T_{\rm rad} = 4000$ K is chosen for modelling the behaviour of T Tauri stars, stars that are in the early stages of formation and shine due to the gravitational energy of their collapse (Appenzeller & Mundt 1989; Natta 1993). The Herbig Ae stars, young A stars still embedded in gas dust envelope, are modelled using the black-body temperature of $T_{\rm rad} = 10\,000$ K (Vioque, M. et al. 2018). The bright and short living B stars are modelled using a black-body temperature of $T_{\rm rad} = 20\,000$ K (Habets & Heintze 1981).

Real fields present a series of absorption lines by species in the atmospheres. Here, we consider real stellar fields for the Sun and Proxima Centauri. The Solar field was taken from Heays et al. (2017) and was compiled from the measurements of Woods et al. (1996) and Curdt et al. (2001); two Proxima Centauri fields are considered, the flux obtained using the PHOENIX model (Husser et al. 2013) and one taken from the MUSCLES treasury survey (France et al. 2016; Loyd et al. 2016; Youngblood et al. 2016, 2017). The MUSCLES data base gives the observational spectrum, reconstructed from different sources (Youngblood et al. 2017) with various correction at low wavelengths. These two fields behave very differently both in shape of the fields themselves and, in the predicted photodissociation rates at essentially all temperatures. We followed Heays et al. (2017) and normalised all radiation field to agree with the integrated energy-intensity of the ISRF radiation field calculated by Draine (1978) between 91.2 and 200 nm ($I_D = 2.6 \times 10^{-10}$ W cm^2).

Fig. 3 compares the PHOENIX and MUSCLES radiation fields for Proxima Centauri with a black-body distribution as function of the wavelength, and the resulting HCl photodissociation rates. The MUSCLES and PHONEIX models differ from the black-body model and each other; the MUSCLES field gives rates which are essentially temperature independent while the PHOENIX field gives rates which increase dramatically with temperature. This figure shows the necessity of using reliable, high-quality UV-visible fluxes in any exoplanetary photochemical model.

3 HCL

The HCl photoabsorption spectrum between 100 and 200 nm (see Fig. 4) is dominated by three different regions: a continuum band centred at 153.64 nm given by the A $^1\Pi \leftarrow$X $^1\Sigma^+$ bound to continuum transitions, a second structured region, between 129 and 120 nm, with contributions from the B $^1\Sigma^+$ ionic bound state, the C $^1\Pi$, and D $^1\Pi$ bound states, and the last region, between 113 and 104 nm, that has contributions from the H $^1\Sigma^+$, K $^1\Pi$, 5 $^1\Pi$, M $^1\Pi$, and 4 $^1\Sigma^+$ bound states. The experimental spectra from Nee, Suto & Lee (1986) and Brion, Dyck & Cooper (2005) are shown as well in Fig. 4, showing

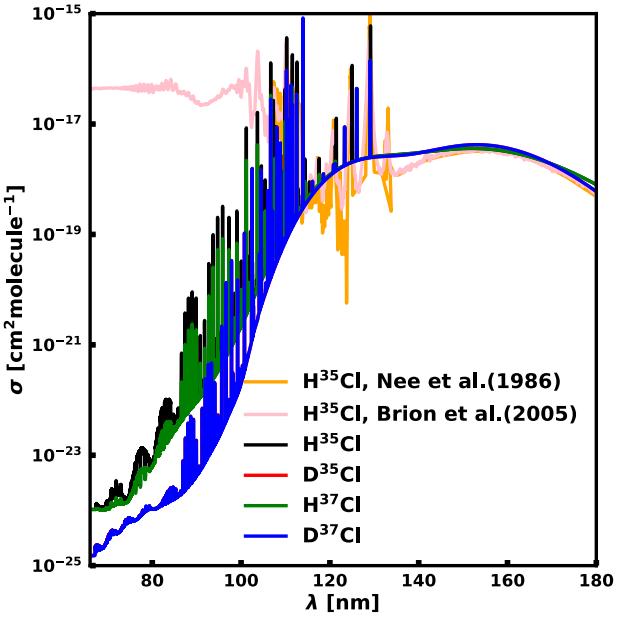

Figure 4. Total photodissociation cross-section of the different isotopologues of HCl at $T = 0$ K. The cross-section tails, for $\lambda < 100$ nm, show the difference between different hydrogen isotopologues: the deuterated species are consistently smaller. The $D^{35}Cl$ spectrum is hidden by the $D^{37}Cl$ spectrum. Experimental cross-sections from Nee et al. (1986) and Brion et al. (2005) are also reported. The difference between the experiments and our model are largely explained by the use of different resolutions. In particular, bound states peak heights depend on the HWHM adopted: they can be several orders of magnitude higher for narrower averaging; however, the integrated cross-section is conserved.

an overall agreement with our model before smoothing is applied to the bound states. The difference between the experiments and our model are largely explained using different resolutions. In particular, bound states peak heights depend on the HWHM adopted: they can be several orders of magnitude higher for narrower averaging; however, the integrated cross-section is conserved.

The first region is dominated by the direct photodissociation from the $A\,^1\Pi$ repulsive electronic state. The A–X band is associated with the HCl→H(^{2}S) + Cl(^{2}P) asymptote. The second region is mainly dominated by the vibrational progression of the $C\,^1\Pi$–$X\,^1\Sigma^+$ band that overlaps with the transitions of the $B\,^1\Sigma^+$–$X\,^1\Sigma^+$ and $D\,^1\Pi$ –$X\,^1\Sigma^+$ photodissociation bands. The dominance of the $C\,^1\Pi$ ←$X\,^1\Sigma^+$ band in this region is driven by its strong transition moment around the equilibrium region of the ground state potential. The $B\,^1\Sigma^+$ ←$X\,^1\Sigma^+$ contribution shows continuum structure, due to the ionic nature of the dissociation limit of this state (HCl→$H^+ + Cl^-$), given by the contributions from the upper minimum at 1.35 Å. The third region is dominated by the $K\,^1\Pi$ ←$X\,^1\Sigma^+$, $M\,^1\Pi$ ←$X\,^1\Sigma^+$, $4\,^1\Sigma^+$ ←$X\,^1\Sigma^+$ bands, with the $5\,^1\Pi$ ←$X\,^1\Sigma^+$ contribution submerged, due to its small cross-section. Given the complexity of the electronic bands in this region, it is not easy to associate single contributions to each of the vibrational progression.

Table 3 compares our results with the experiments of Nee et al. (1986), Cheng et al. (2002), and Li et al. (2006), and theoretical studies of van Dishoeck et al. (1982) and Engin et al. (2012) for $H^{35}Cl$. Table 4 presents a similar comparison with experiment of Cheng et al. (2002) for $D^{35}Cl$. We assume a temperature of $T = 0$ K for these comparisons and use the oscillator strengths (f) instead of cross-sections, in order to have a direct comparison with the previous studies. The conversion between cross-sections and oscillator strength is made using the same formulation of Cheng et al. (2002):

$$f = 1.13 \times 10^{12} \int_{\nu_1}^{\nu_2} \sigma(\nu) \mathrm{d}\nu \tag{5}$$

where ν_1 and ν_2 are the integration limits, in wavenumbers, for a given peak.

The $A\,^1\Pi$ ←$X\,^1\Sigma^+$ peak position and f agree within ±0.19 nm and 3.0×10^{-3}, respectively, with the experimental values from Cheng et al. (2002). There is a discrepancy between the experimental and calculated peak position values for $D^{35}Cl$, as our λ_{max} is blueshifted by 1.74 nm. The transitions involving the $C\,^1\Pi$ state are experimentally available for multiple vibrational states for the hydrogen isotopes. For both isotopologues, our vibrational overtone positions of the excited state are more closely spaced than those observed experimentally. The oscillator strengths of the $D\,^1\Pi$ ←$X\,^1\Sigma^+$, $H\,^1\Sigma$ ←$X\,^1\Sigma^+$, $K\,^1\Pi$ ←$X\,^1\Sigma^+$, $M\,^1\Pi$ ←$X\,^1\Sigma^+$, $4\,^1\Sigma$ ←$X\,^1\Sigma^+$ bands agree with the results of Engin et al. (2012). However, the oscillator strength of the $5\,^1\Pi$ ←$X\,^1\Sigma^+$ band is two orders of magnitude lower than the values of Engin et al. (2012).

The effects of isotopic substitution on the photoabsorption spectrum of HCl are shown in Fig. 4. The major isotopic effect is present in the short wavelength tail of the photoabsorption spectrum. The cross-sections for hydrogenated species are systematically higher than deuterated for $\lambda \leq 110$ nm, and the spacing of the vibrational progression of hydrogenated species is higher than that encountered for deuterated species.

Fig. 5 presents the temperature dependence of the partial and total cross-sections, by showing cross-sections at $T = 0$, $T = 500$, $T = 3000$, and $T = 10\,000$ K. The $D\,^1\Pi$ ←$X\,^1\Sigma^+$ and the $5\,^1\Pi$ ←$X\,^1\Sigma^+$ bands are excluded from the figure for sake of clarity, because their contributions are below 10^{-18} cm^2 molecule^{-1}. There is no major difference between the cross-sections at $T = 0$ and $T = 500$ K, while major changes are observed above $T = 3000$ K. There is an increase of the cross-section tails at long wavelengths, as more excited vibrational states are accessible at high temperatures. At $T = 10\,000$ K, the $B^1\Sigma^+$ ←$X\,^1\Sigma^+$ band shows two peaks. They correspond to two different minima of the $B^1\Sigma^+$ electronic state potential, as the minimum at $r_{HCl} = 2.44$ Å becomes accessible at high temperatures. Increasing the temperature results in a degradation of the vibrational progressions and to a general redshift, of the order of 10–15 nm for the $C\,^1\Pi$ ←$X\,^1\Sigma^+$ transitions. The same group of transitions shows a change of the peak intensities in the vibrational progression, as the $C\,^1\Pi(v = 1)$ ← $X\,^1\Sigma^+(v = 0)$ transition becomes stronger than the $C\,^1\Pi(v = 0)$ ←$X\,^1\Sigma^+(v = 0)$ at $T = 3000$ K. The vibrational progression at 114.69 nm shows a general redshift for $T \leq 3000$ K, with the effect changing depending on the electronic state under examination: the $K\,^1\Pi$ ←$X\,^1\Sigma^+$ and $M\,^1\Pi$ ←$X\,^1\Sigma^+$ bands show a shift up to 5 nm, the $4\,^1\Sigma^+$ ←$X\,^1\Sigma^+$ band increases up to 20 nm, while the $H^1\Sigma^+$ ←$X\,^1\Sigma^+$ band shifts for values above 25 nm.

Fig. 6 shows how the photodissociation rates change as function of temperature for $H^{35}Cl$. The stellar field influences the temperature dependence of the photodissociation rate. Fields due to high temperature stars tend to flatten the temperature effects on the rates: for ISRF and 20 000 K they are constant within 10 per cent for all practical purposes. Considering the black-body radiation at 4000 K, the photodissociation rate increases 213 times from 100 to 10 000 K. For the same temperature interval, the radiation field generated by a black-body at 20 000 K shows an increase by a factor of only 1.32. The most dramatic temperature effect is observed for the PHOENIX model stellar field of Proxima Centuari: the curve shows

Table 3. Comparison between electronic transitions of HCl presented by van Dishoeck et al. (1982), Nee et al. (1986), Cheng et al. (2002), Li et al. (2006), Engin et al. (2012), and our values. For each electronic state the vibronic progression, the peak position the oscillator strength, f, are given.

State	Transition	$\lambda_{\text{vanDishoeck}}$ (nm)	λ_{Nee} (nm)	λ_{Cheng} (nm)	λ_{Li} (nm)	λ_{Engin} (nm)	λ (nm)	$f_{\text{vanDishoeck}}$ (unitless)	f_{Nee} (unitless)	f_{Cheng} (unitless)	f_{Li} (unitless)	f_{Engin} (unitless)	f (unitless)
$A\,^1\Pi$	broad	–	–	153.83	–	156.94	153.64	–	–	5.1×10^{-2}	4.2×10^{-2}	7.06×10^{-2}	5.4×10^{-2}
$C\,^1\Pi$	$0 \rightarrow 0$	128.88	129.02	129.15	129.02	131.20	129.16	1.5×10^{-1}	1.3×10^{-1}	1.3×10^{-1}	1.5×10^{-1}	1.4×10^{-1}	1.5×10^{-1}
	$0 \rightarrow 1$	124.61	124.36	124.73	124.73	127.03	125.03	2.4×10^{-2}	1.7×10^{-2}	1.7×10^{-2}	2.0×10^{-2}	3.0×10^{-2}	2.7×10^{-2}
	$0 \rightarrow 2$	120.84	120.72	120.84	120.84	123.37	121.45	2.4×10^{-3}	2.6×10^{-3}	2.6×10^{-3}	4.1×10^{-1}	5.6×10^{-3}	2.7×10^{-3}
	$0 \rightarrow 3$	117.41	–	–	–	120.14	118.27	6.0×10^{-5}	–	–	–	8.0×10^{-4}	1.6×10^{-5}
$B\,^1\Sigma^+$	broad	–	–	–	–	130.92	128.68	–	–	–	–	0.0	3.1×10^{-2}
$D\,^1\Pi$	$0 \rightarrow 0$	–	–	–	–	124.61	121.24	–	–	–	–	9.0×10^{-4}	6.3×10^{-4}
$H\,^1\Sigma^+$	$0 \rightarrow 0$	–	112.61	–	112.82	114.69	112.61	–	1.0×10^{-2}	–	1.1×10^{-2}	3.2×10^{-2}	3.2×10^{-2}
	$0 \rightarrow 1$	–	–	–	–	112.41	109.94	–	–	–	–	7.8×10^{-3}	1.0×10^{-2}
	$0 \rightarrow 2$	–	–	–	–	110.21	107.59	–	–	–	–	3.3×10^{-4}	2.0×10^{-4}
$K\,^1\Pi$	$0 \rightarrow 0$	–	111.40	–	111.60	114.27	111.56	–	2.1×10^{-2}	–	–	2.7×10^{-2}	4.3×10^{-2}
	$0 \rightarrow 1$	–	–	–	–	111.00	108.07*	–	–	–	–	2.3×10^{-3}	1.4×10^{-3}
$5\,^1\Pi$	$0 \rightarrow 0$	–	–	–	–	113.85	111.00	–	–	–	–	5.0×10^{-5}	8.0×10^{-7}
$M\,^1\Pi$	$0 \rightarrow 0$	–	110.21	–	110.31	113.23	110.27	–	3.2×10^{-2}	–	1.3×10^{-1}	8.5×10^{-2}	8.7×10^{-2}
	$0 \rightarrow 1$	–	–	–	–	110.11	107.28	–	–	–	–	6.4×10^{-3}	6.3×10^{-3}
	$0 \rightarrow 2$	–	–	–	–	107.35	104.58	–	–	–	–	5.0×10^{-4}	4.1×10^{-4}
$4\,^1\Sigma^+$	$0 \rightarrow 0$	–	–	–	–	110.60	106.68	–	–	–	–	3.2×10^{-2}	3.0×10^{-2}

Table 4. Comparison between electronic transitions presented by Cheng et al. (2002), and our values for DCl. For each electronic state the vibronic progression, the peak position, and the oscillator strength, *f*, are given.

State	Transition	$\lambda_{\rm Cheng}$ (nm)	λ (nm)	$f_{\rm Cheng}$ (unitless)	f (unitless)
$A\,^1\Pi$	broad	155.76	154.02	4.9×10^{-2}	5.4×10^{-2}
$C\,^1\Pi$	$0 \rightarrow 0$	129.15	129.11	1.3×10^{-1}	1.3×10^{-1}
	$0 \rightarrow 1$	125.87	126.06	1.7×10^{-2}	3.9×10^{-2}
	$0 \rightarrow 2$	122.88	123.37	3.3×10^{-3}	6.0×10^{-3}
	$0 \rightarrow 3$	120.26	120.84	7.0×10^{-4}	3.0×10^{-4}
$D\,^1\Pi$	$0 \rightarrow 0$	121.20	121.20	6.0×10^{-4}	4.9×10^{-4}

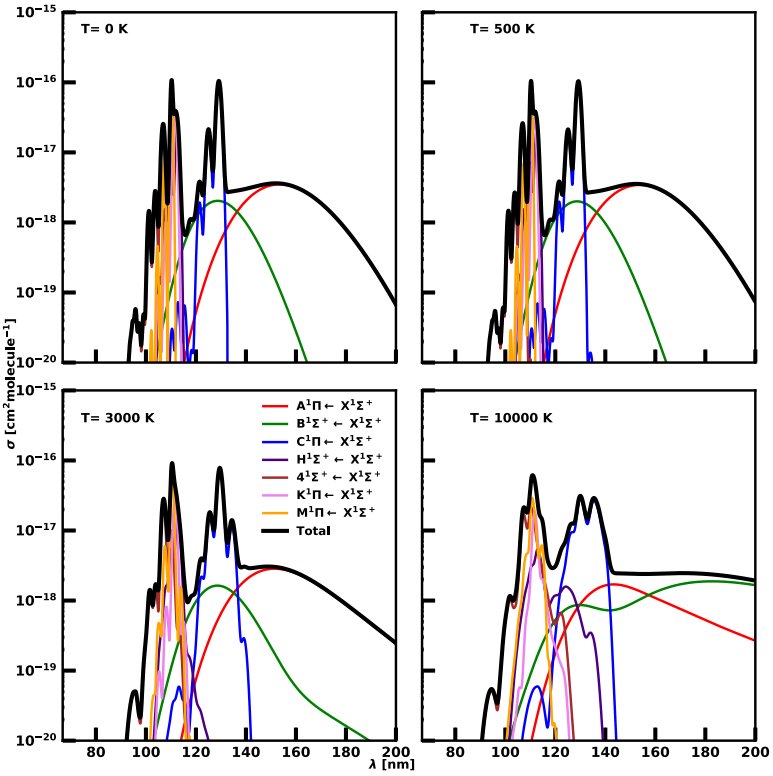

Figure 5. Total and partial photodissociation cross-sections of $H^{35}Cl$ at 0, 500, 3000, and 10 000 K. The $D\,^1\Pi$ and the $5\,^1\Pi$ states are excluded, due to their contributions being below 10^{-18} cm^2 molecule^{-1}. The total spectrum is composed of a broad-band given by the $A\,^1\Pi \leftarrow X\,^1\Sigma^+$ at 153.64 nm, a discrete progression derived by the $C\,^1\Pi \leftarrow X\,^1\Sigma^+$ at 129.16 nm and another set of discrete transitions starting at 112.61 nm, given by the contribution of the other excited states.

an exponential behaviour for temperatures above 1000 K; this effect leads to an increase by 7.36×10^7 times from 100 K to 10 000 K. The MUSCLES field for Proxima Centauri shows completely different behaviour to the PHOENIX model, with essentially no variation with temperature.

The effect of isotopic substitution is illustrated in Table 5. $H^{37}Cl$ and $D^{37}Cl$ show similar temperature behaviour to $H^{35}Cl$ in Fig. 6 for all stellar fields. The rates of $D^{35}Cl$ using the 4000 K black-body field are anomalous compared to the others, as it shows a rapid increase with temperature giving a rate one order of magnitude higher at 10 000 K.

van Dishoeck et al. (1982) estimated photodissociation rates in the ISRF stellar field for HCl. Their model, which included 5 singlet states and 5 triplet states, gave a total photodissociation rate of 9.81×10^{-10} s^{-1}, lower than our value of 1.23×10^{-9} s^{-1}. This difference is due to the exclusion in their models of excited states above 113 nm. They reported the single state contribution from the $A\,^1\Pi \leftarrow X\,^1\Sigma$, and the $C\,^1\Pi \leftarrow X\,^1\Sigma$ transitions. Their values, 2.1×10^{-10} and 5.3×10^{-10} s^{-1}, respectively, agree within the 10 per cent with our values, 2.3×10^{-10} and 5.2×10^{-10} s^{-1}, respectively. The total photodissociation rates at $T = 0$ K are in good agreement with those reported by Heays et al. (2017). Our rates for the ISRF, Solar, and the black-body at 4000, 10 000, and 20 000 K are 1.23×10^{-9}, 1.57×10^{-10}, 1.43×10^{-10}, 5.36×10^{-10}, and 1.06×10^{-9} s^{-1}, versus 1.73×10^{-9}, 1.08×10^{-10}, 9.35×10^{-11}, 5.06×10^{-10}, and 1.47×10^{-9} s^{-1} reported in the data base.

4 HF

The photodissocation spectrum of HF is characterized by two regions: the continuum band centred at 120.09 nm given by the $A\,^1\Pi \leftarrow X\,^1\Sigma^+$ transitions, the second structured region between 95

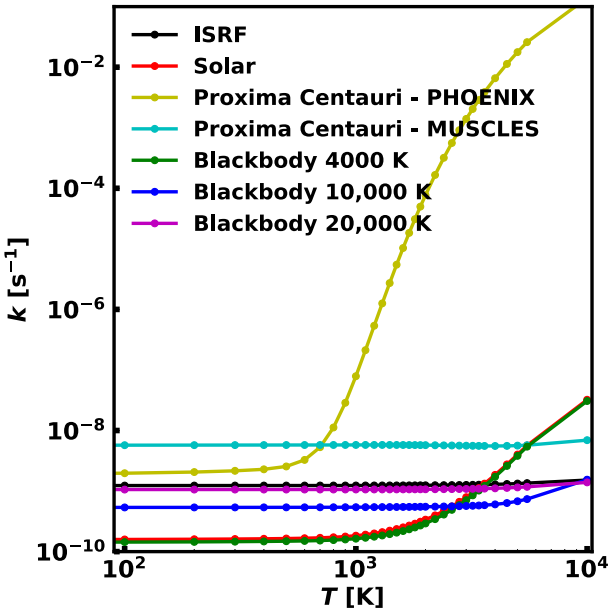

Figure 6. Photodissociation rates of $H^{35}Cl$ between 100 and 10 000 K for different stellar fields. The ISRF is in black, the Solar field in red, the Proxima Centauri field with the PHOENIX model (Husser et al. 2013) in yellow, the Proxima Centauri field with the MUSCLES model (Youngblood et al. 2017) in cyan; the blackbody temperatures are in green (4000 K), in blue (10 000 K), and in violet (20 000 K). The temperature dependence of the photodissociation rates depends strongly on the stellar field, the higher the stellar field temperature, the lower is the increase in photodissociation rate as function of molecular temperature. The photodissociation rates for the ISRF and the blackbody at 20 000 K do not show appreciable temperature dependence, while the Solar and the blackbody at 4000 K increase by a factor of 213 within the temperature interval considered. The rates obtained using the Proxima Centauri field with the PHOENIX model show a dramatic temperature effect, with a change in rates of the order of 10^7.

and 80 nm, with the main contribution from the $C\,^1\Pi$ state, and the $B\,^1\Sigma^+$–$X\,^1\Sigma^+$ band, that is submerged below the C–X band.

Experiments reporting the HF photoabsorption are due to Hitchcock et al. (1984), who describes different electronic transitions, and Nee et al. (1985) who reports cross-section for the $A\,^1\Pi \leftarrow X\,^1\Sigma^+$ only. The MPI-Mainz data base also cites the experimental data from Carnovale, Tseng & Brion (1981) and host their photoabsorption cross-sections of HF, the agreement with their data is less good, given lower experimental resolution. Table 6 compares our peak positions and oscillator strengths of HF with experimental data from Hitchcock et al. (1984). Our calculations agree with the $A\,^1\Pi \leftarrow X\,^1\Sigma^+$ band reported by Nee et al. (1985) with a peak position at $\lambda = 121.70$ nm, cross-section of 3.3×10^{-18} cm^2 molecule^{-1} and $f = 4.6 \times 10^{-2}$. Nee et al.'s measurements give a cross-sections a factor of 0.53 lower than the experiments of Hitchcock et al. (1984), but which agrees with our calculations and with the theoretical results of Brown & Balint-Kurti (2000). Our peak positions and oscillation strengths for the $C\,^1\Pi \leftarrow X\,^1\Sigma^+$ transitions are in a good agreement with Hitchcock et al. (1984), while the oscillator strengths for the $A\,^1\Pi \leftarrow X\,^1\Sigma^+$ and the $B\,^1\Sigma^+ \leftarrow X\,^1\Sigma^+$ differ by a factor of 0.50 and 0.56, respectively, supporting the experiments of Nee et al. (1985). Considering the good agreement between our methodology and experiments for HCl, we suppose that the experimental data from Hitchcock et al. (1984) could have some problem in assigning transitions of different nature (continuum *versus* discrete).

The temperature effect on the HF cross-sections is illustrated in Fig. 7. As in the case of HCl, there are no major differences between spectra between 0 and 500 K. We observe a change in the $C\,^1\Pi \leftarrow X\,^1\Sigma^+$ vibrational progression, that shifts to energy values above 100 nm, and the increase of the energy tail for high wavelengths, mainly from the $A\,^1\Pi \leftarrow X\,^1\Sigma^+$ band.

The computational work of Brown & Balint-Kurti (2000) is the only source of information available for the $A\,^1\Pi \leftarrow X\,^1\Sigma^+$ band of DF. They reported that the photodissociation cross-section of DF peaked at higher wavelengths with a higher peak and narrower

Table 5. Photodissociation rates for all HCl isotopologues at blackbody temperatures of 100, 1500, 3000, 5000, and 10 000 K.

Blackbody field	Isotopologue	k(100 K) (s^{-1})	k(1500 K) (s^{-1})	k(3000 K) (s^{-1})	k(5000 K) (s^{-1})	k(10000 K) (s^{-1})
4000 K	$H^{35}Cl$	1.44×10^{-10}	2.06×10^{-10}	7.07×10^{-10}	3.81×10^{-9}	3.07×10^{-8}
	$D^{35}Cl$	1.14×10^{-10}	3.34×10^{-9}	2.32×10^{-8}	6.51×10^{-8}	2.04×10^{-7}
	$H^{37}Cl$	1.43×10^{-10}	2.06×10^{-10}	7.07×10^{-10}	3.81×10^{-9}	3.07×10^{-8}
	$D^{37}Cl$	1.08×10^{-10}	1.76×10^{-10}	6.70×10^{-10}	3.74×10^{-9}	3.00×10^{-8}
10 000 K	$H^{35}Cl$	5.37×10^{-10}	5.46×10^{-10}	5.67×10^{-10}	6.79×10^{-10}	1.54×10^{-9}
	$D^{35}Cl$	5.46×10^{-10}	5.83×10^{-10}	7.03×10^{-10}	9.64×10^{-10}	2.04×10^{-9}
	$H^{37}Cl$	5.35×10^{-10}	5.45×10^{-10}	5.67×10^{-10}	6.79×10^{-10}	1.54×10^{-9}
	$D^{37}Cl$	5.37×10^{-10}	5.47×10^{-10}	5.69×10^{-10}	6.79×10^{-10}	1.53×10^{-9}
20 000 K	$H^{35}Cl$	1.05×10^{-9}	1.07×10^{-9}	1.08×10^{-9}	1.15×10^{-9}	1.39×10^{-9}
	$D^{35}Cl$	1.12×10^{-9}	1.13×10^{-9}	1.16×10^{-9}	1.25×10^{-9}	1.50×10^{-9}
	$H^{37}Cl$	1.06×10^{-9}	1.07×10^{-9}	1.08×10^{-9}	1.15×10^{-9}	1.39×10^{-9}
	$D^{37}Cl$	1.07×10^{-9}	1.07×10^{-9}	1.09×10^{-9}	1.15×10^{-9}	1.40×10^{-9}

Table 6. Comparison between electronic transitions presented by Hitchcock et al. (1984), and our values. for the deuterated species. For each electronic state we are reporting the vibronic progression, the peak position, and the oscillator strength, f.

State	Transition	$\lambda_{\rm Hitchcock}$ (nm)	λ (nm)	$f_{\rm Hitchcock}$(unitless)	f (unitless)
$A\,^1\Pi$	broad	119.79	119.78	9.8×10^{-2}	4.9×10^{-2}
$B\,^1\Sigma^+$	broad	93.93	93.93	2.5×10^{-2}	1.4×10^{-2}
$C\,^1\Pi$	$0 \rightarrow 0$	95.15	95.17	5.6×10^{-2}	5.7×10^{-2}

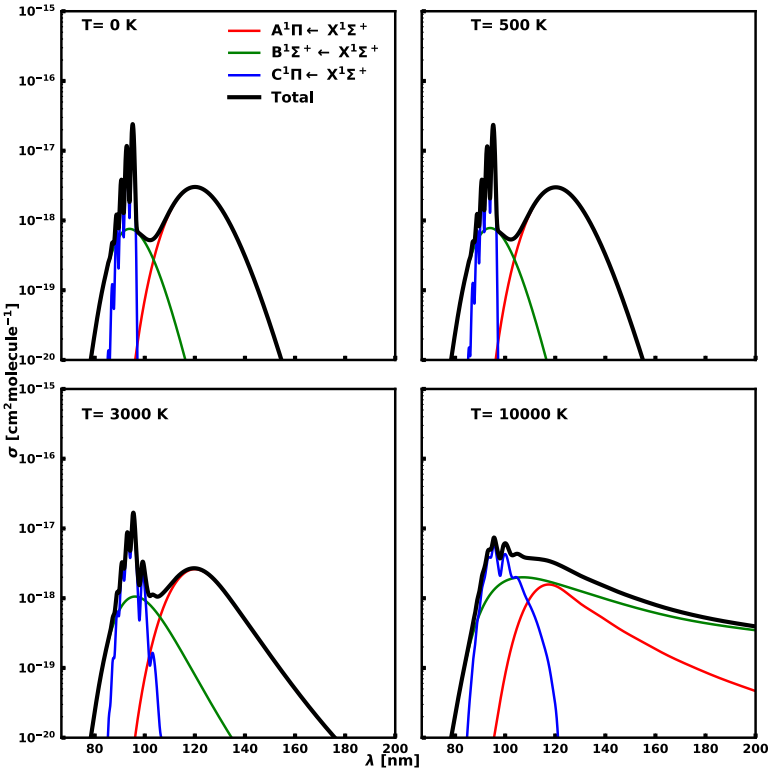

Figure 7. Total and partial photodissociation cross-sections of HF at 0, 500, 3000, and 10 000 K. The total spectrum is composed of a broad band given by $A\,^1\Pi \leftarrow X\,^1\Sigma^+$ at 120.09 nm, and a discrete progression of $C\,^1\Pi \leftarrow X\,^1\Sigma^+$ at 95.17 nm.

profile. Our data shows a similar behaviour, with a difference of 2.20 nm between the cross-sections of HF and DF. The spacing between the $C\,^1\Pi \leftarrow X\,^1\Sigma^+$ vibrational progression is smaller than in HF, due to the increase of mass of the deuterated species. Fig. 8 shows the cross-sections of the two isotopes together with the experimental data from Carnovale et al. (1981) and Nee et al. (1985).

HF photodissociation rates for different radiation fields are plotted in Fig. 9. The temperature dependence of the black-body field at 20 000 K and the ISRF is similar to those observed for HCl: they have a similar temperature dependence, and increase by a factor of 2.66 as T increases from 100 to 10 000 K. More significant differences between HCl and HF are encountered for the black-body radiation field at 4000 K and the Proxima Centauri fields. For temperatures below 2000 the 4000 K field is two orders of magnitude smaller than the solar field, in contrast to the case of HCl, where the fields have the same trend. There is a sudden increase in the rates from 2000 K, with the Solar and the 4000 K black-body field showing the same trend after 4000 K. Rates computed using the Proxima Centauri field with the PHOENIX model show the greatest increase in the temperature range: 9×10^{13} times, from 100 to 10 000 K.

Table 7 shows the isotopic dependence of the photodissociation rate of HF and DF. For both isotopes, the 10 000 and 20 000 K black-body fields have the same temperature dependence photodissociation rates. In case of the black-body field at 4000 K, we observe that the deuterated isotopologue shows rates one order of magnitude lower than for HF, for temperatures below 3000 K, but rapidly increases for higher temperature: the ratio between $k_{\rm DF}(10\,000)$ and $k_{\rm HF}(10\,000)$ is 0.61. Also, for HF, total photodissociation rates at $T = 0$ K agree with the ones reported by Heays et al. (2017). Our rates for the ISRF, Solar, and the black-body at 4000 K, 10 000 and 20 000 K

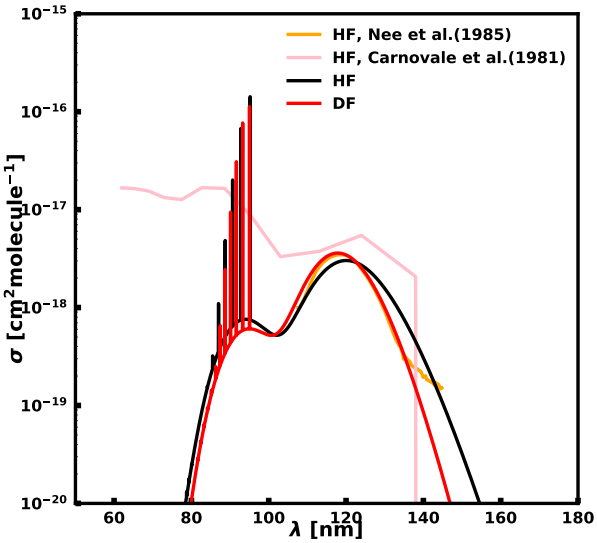

Figure 8. Total photodissociation cross-section of HF and DF at $T = 0$ K. The $A\,^1\Pi \leftarrow X\,^1\Sigma^+$ band shows a shift of 2.20 nm between the hydrogenated and the deuterated species. The spacing between the $C\,^1\Pi \leftarrow X\,^1\Sigma^+$ vibrational progression is smaller than that observed in HF. These spectra are compared with the experimental results from Carnovale et al. (1981) and Nee et al. (1985); in both cases the scarcity of experimental data is evident: in case of Carnovale et al. (1981) the sampling is too coarse to discern the vibrational progressions from the bound states, while Nee et al. (1985) report the contribution of the $A\,^1\Pi \leftarrow X\,^1\Sigma^+$ band. Bound states peak heights depend on the Gaussian smoothing function adopted: they can be several orders of magnitude higher with narrower averaging; however, the integrated cross-section is conserved.

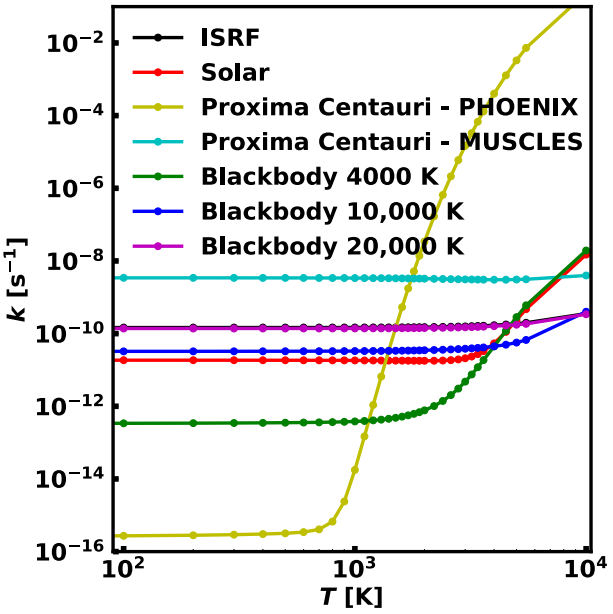

Figure 9. Photodissociation rates between 100 and 10 000 K for different stellar fields of HF. The ISRF is in black, the Solar field in red, the Proxima Centuary with the PHOENIX model (Husser et al. 2013) in yellow, the Proxima Centuary with the MUSCLES model (Youngblood et al. 2017) in cyan; the blackbody temperatures are in green (4000 K), in blue (10 000 K), and in violet (20 000 K). The temperature dependence of the photodissociation rates depends strongly on the stellar field, the higher is the stellar field temperature, the lower is the increase of the photodissociation rate as function of temperature. The photodissociation rates for the ISRF and the blackbody at 20 000 K and the MUSCLES model is essentially independent of temperature, while the Solar and the blackbody at 4000 K increase of a factor of ∼250 within the temperature interval. The ISRF and the blackbody at 20 000 K curves overlap through the entire temperature interval. The Proxima Centauri field with the PHOENIX model shows the strongest temperature dependence, with an increase of 9×10^{13} times within the temperature range.

are 1.47×10^{-10}, 1.86×10^{-11}, 3.37×10^{-13}, 3.24×10^{-11}, and 1.38×10^{-10} s^{-1}, versus 1.38×10^{-10}, 2.18×10^{-11}, 5.31×10^{-13}, 2.88×10^{-11}, and 1.17×10^{-10} s^{-1} reported in the data base.

5 DATA PROVISION

A new data type called photodissociation cross-sections (cm^2 molecule^{-1}) has been created in the ExoMol data base, www.exomol.com (Tennyson et al. 2016), based on the ExoMol data structure described by Hill, Yurchenko & Tennyson (2013). For each isotopologue, a new entry will be added in the definition file supplementing the states and transitions file structure used to present line lists. In accordance with the ExoMol convention, the photodissociation data are not scaled with the isotopic abundance. The photodissociation cross-sections will be published with low resolutions (1.0 nm) and high resolution (0.1 nm) spacing for the temperatures given in Table 1; results for the present calculations will cover wavelengths between 100 and 400 nm with no pressure effects considered. Cross-sections are stored in form of a space separated variable file. The file is structured as follows; the first column shows the wavelength, the second column reports the total cross-section. The different temperature contributions are separated by a blank line. Table 8 shows as example the first four lines of $H^{35}Cl(T = 0$ K) for the 1 nm spacing, the last two lines of $H^{35}Cl(T = 0$ K) with the first four lines of $H^{35}Cl(T = 100$ K). The line above the data shows the data formatting. The total and partial cross-sections contributions are reported in the electronic supporting information, with a small sample reported in Table 9.

It is relatively easy to generate photodissociation rates as a function of molecular temperature from the tabulated cross-sections using a specified radiation field and equation (1). It is our plan to implement an automated procedure to do this alongside a library of appropriate radiation fields.

Table 8. Header of photodissociation cross-section file for $H^{35}Cl$ at $T = 0$ K for the 1 nm spacing, also shown are the last two lines for $T = 0$ K and the first four lines for $T = 100$ K. Wavelengths (λ) are in nm, and cross-sections (σ) in cm^2 molecule^{-1}. The first line gives the formatting used to write the data.

λ	σ^{Total}
F6.2	es13.5
100.00	4.85536E−20
101.00	1.11513E−19
102.00	1.37037E−18
103.00	4.82263E−19
104.00	1.21327E−18
⋮	⋮
399.00	0.00000E+00
400.00	0.00000E+00
100.00	5.06233E−20
101.00	1.10736E−19
102.00	1.36532E−18
103.00	4.99004E−19
104.00	1.18854E−18

6 CONCLUSIONS

In this paper, we present the first in a series of papers investigating the temperature dependence of the photodissociation cross-sections and rates for molecules of importance to exoplanetary, and of course other, studies. In this work we focus on two hydrogen halides, HCl and HF, and their isotopologues.

Table 7. Photodissociation rates for black-body temperatures of HF and DF at 100, 1500, 3000, 5000, and 10 000 K.

Field	Isotopologue	k(100 K) (s^{-1})	k(1500 K) (s^{-1})	k(3000 K) (s^{-1})	k(5000 K) (s^{-1})	k(10000 K) (s^{-1}))
Black-body 4000 K	HF	3.40×10^{-13}	4.82×10^{-13}	4.76×10^{-12}	2.84×10^{-10}	1.94×10^{-8}
	DF	5.71×10^{-14}	8.82×10^{-14}	1.02×10^{-12}	1.20×10^{-10}	1.19×10^{-8}
Black-body 10 000 K	HF	3.25×10^{-11}	3.38×10^{-11}	3.83×10^{-11}	5.67×10^{-11}	4.00×10^{-10}
	DF	1.97×10^{-11}	2.07×10^{-11}	2.41×10^{-11}	3.86×10^{-11}	3.37×10^{-10}
Black-body 20 000 K	HF	1.38×10^{-10}	1.40×10^{-10}	1.49×10^{-10}	1.76×10^{-10}	3.41×10^{-10}
	DF	1.15×10^{-10}	1.18×10^{-10}	1.27×10^{-10}	1.52×10^{-10}	3.06×10^{-10}

Table 9. Header of the photodissociation cross-section table presented in the Supporting Information for $H^{35}Cl$ for $T = 0$ K for the 1 nm spacing, plus the last two lines for $T = 0$ K and the first four for $T = 100$ K. Wavelengths (λ) are in nm, and cross-sections (σ) in cm^2 molecule^{-1}. The first line reports the formatting used for writing the data.

λ	$\sigma^{\rm Total}$	$\sigma^{A\,^1\Pi\leftarrow X\,^1\Sigma^+}$	$\sigma^{C\,^1\Pi\leftarrow X\,^1\Sigma^+}$	$\sigma^{B\,^1\Sigma^+\leftarrow X\,^1\Sigma^+}$	$\sigma^{D\,^1\Pi\leftarrow X\,^1\Sigma^+}$	$\sigma^{H\,^1\Sigma^+\leftarrow X\,^1\Sigma^+}$	$\sigma^{K\,^1\Pi\leftarrow X\,^1\Sigma^+}$	$\sigma^{5\,^1\Pi\leftarrow X\,^1\Sigma^+}$	$\sigma^{M\,^1\Pi\leftarrow X\,^1\Sigma^+}$	$\sigma^{4\,^1\Sigma^+\leftarrow X\,^1\Sigma^+}$
1x,F6.2	10 ×(1x,es13.5)									
100.00	4.85536E−20	2.49720E−25	7.385653E−23	1.438835E−21	1.16735E−22	1.37962E−21	2.14801E−22	1.96018E−22	2.35598E−23	4.51099E−20
101.00	1.11513E−19	7.06771E−25	1.918758E−22	2.143218E−21	1.83478E−22	5.26944E−21	9.95494E−22	1.75402E−21	1.74545E−21	9.92297E−20
102.00	1.37037E−18	1.86128E−24	4.206999E−22	3.240703E−21	5.461986E−23	3.33646E−21	1.76091E−22	8.89503E−22	8.28554E−23	1.36217E−18
103.00	4.82263E−19	4.52986E−24	3.515567E−22	4.953732E−21	1.11922E−23	5.20284E−21	7.70287E−22	2.39150E−21	2.65150E−20	4.42062E−19
104.00	1.21327E−18	1.04052E−23	5.363629E−22	7.578607E−21	2.68010E−22	9.32299E−22	4.91039E−22	3.03492E−21	1.13187E−21	1.19929E−18
					⋮					
399.00	0.00000E + 00	0.00000E + 00	0.000000E + 00	0.000000E + 00	0.00000E + 00	0.000000E + 00	0.00000E + 00	0.00000E + 00	0.000000E + 00	0.000000E + 00
400.00	0.00000E + 00	0.00000E + 00	0.000000E + 00	0.000000E + 00	0.00000E + 00	0.000000E + 00	0.00000E + 00	0.00000E + 00	0.000000E + 00	0.000000E + 00
100.00	5.06233E−20	2.47899E−25	7.34458E−23	1.44117E−21	1.22165E−22	1.415554E−21	2.14494E−22	2.01564E−22	2.24269E−23	4.71323E−20
101.00	1.10736E−19	7.02051E−25	1.97132E−22	2.14565E−21	1.78191E−22	5.281147E−21	9.81729E−22	1.73214E−21	1.76048E−21	9.84586E−20
102.00	1.36532E−18	1.84883E−24	4.16114E−22	3.24302E−21	5.790111E−23	3.281736E−21	1.83332E−22	9.18835E−22	8.15775E−23	1.35714E−18
103.00	4.99004E−19	4.49979E−24	3.48161E−22	4.95397E−21	1.36449E−23	5.242623E−21	7.99597E−22	2.32904E−21	2.62712E−20	4.59041E−19
104.00	1.18854E−18	1.03338E−23	5.43194E−22	7.57846E−21	2.57864E−22	1.063908E−21	5.15449E−22	3.05713E−21	1.25755E−21	1.17425E−18

In case of HCl, we have considered 9 singlet electronic bands from the ground electronic state of the four main isotopes $H^{35}Cl$, $D^{35}Cl$, $H^{37}Cl$, and $D^{37}Cl$. We observe that an increase in temperature leads to the loss of details of bound–bound transitions and an increase in the cross-sections at high wavenumber, given by the population of higher rotational and vibrational states in the electronic ground state. We calculate the photodissociation rates for five different stellar fields, corresponding to the ISRF, Solar spectrum, and three different black-body fields. We observe that the dissociation rate in stellar fields corresponding to low-temperature stars shows a large dependence on the molecular temperature, of at least two orders of magnitudes; the hot temperature fields instead are less sensitive to the temperature. The isotopic effect is prominent in the case of DCl, that, in case of 4000 K black-body radiation field, shows a variation of the photodissociation rate of two/one order of magnitude at $T >$ 3000 K.

We studied the electronic photodissociation spectrum between the electronic ground state and the first 3 electronic excited states of HF and DF. The photoabsorption cross-sections show similar characteristics to HCl, but with the electronic states more separated than HCl. The photodissociation rates for the ISRF and black-body fields at 10 000 and 20 000 K show the same temperature trend as HCl, while the black-body field of 4000 K shows completely different behaviour at low temperatures with respect to the Solar field: the rates obtained using the black-body of 4000 K are two orders of magnitude lower than the rates obtained by the Solar field.

The rapid rise in photodissociation rates with temperature in typical radiation fields of cool stars is important. This process is largely driven by the fact that in general vibrational excitation leads to a lowering of the photodissociation threshold which is typically several times larger than the vibrational excitation energy involved, see Stibbe & Tennyson (1998) for a discussion of this. HF and HCl actually have quite large vibrational quanta meaning that thermal vibrational excitation only becomes significant at temperatures over 3000 K. For most other molecules of importance for exoplanetary atmospheres one would expect the sharp rise in photodissociation rates to start at lower temperatures due to their smaller spacing between vibrational levels. However, we show that, particularly for cool stars, the precise form of the stellar radiation field used in any model may be crucial in obtaining reliable results. This finding, together with the recent work from Teal et al. (2022), put emphasis on the need to correctly characterize these fields.

The discussion of rates in this paper is based entirely on the assumption that the molecule concerned is thermalized. However, non-local thermodynamic equilibrium (NLTE) effects are thought to be important in exoplanets. It would be relatively straightforward to adapt our procedure to provide NLTE data, but this would require re-summing individual vibrational and rotational contributions to the cross-sections.

Our photodissociation models for HCl and HF are based on two assumptions. The first assumption is that every excitation leads to a dissociative event, as discussed in the methods section. The second assumption concerns the use of the adiabatic B $^1\Sigma^+$ for HCl instead of the diabatic V $^1\Sigma^+$ ionic and E $^1\Sigma^+$ Rydberg states. While this choice is justified in case of photodissociation, it may not be optimal for building a spectroscopic model, as shown by the high resolution REMPI spectra of Green, Bickel & Wallace (1991). In this case, the rovibrational levels spacing of the two states become an important factor to consider. The E $^1\Sigma^+$ rotational constants are comparable to the X $^1\Sigma^+$ ones, while the V $^1\Sigma^+$ rotational constants are smaller by a factor of two (Ginter & Ginter 1981; de Beer et al. 1990; Green et al. 1991; Long, Wang & Kvaran 2013). Similarly, to

obtain details of the product distribution it is necessary to consider the singlet-triplet couplings. The triplet states (a $^3\Pi$, b $^3\Pi$, t $^3\Sigma^+$, *etc*...) are important for final product states analysis (Alexander et al. 1998; Regan et al. 1999, 2000). Implementation of model which includes triplet states and the appropriate spin–orbit couplings would allow final state analysis of photodissociation processes to be performed which would improve our understanding of these phenomena, and it will help in the understanding of the tiplet excitation contributions for vibrationally excited molecules, quantifying their overall contributions for high temperatures. This problem is left to future work.

ACKNOWLEDGEMENTS

We thank Olivia Venot for helpful discussions over the course of this work. This work was funded by ERC Advanced Investigator Project 883830 and by the STFC Project ST/R000476/1.

DATA AVAILABILITY

DUO and EXOCROSS input files HCl and HF as used for generating the photodissociation cross-sections and rates are available as supplementary information in archives *HCl.zip* and *HF.zip*. The open access programs DUO and EXOCROSS are available from github.com/exomol.

The computed photodissociation cross-sections are available from the ExoMol website, www.exomol.com and as supplementary material to this paper.

REFERENCES

Alexander M. H., Pouilly B., Duhoo T., 1993, J. Chem. Phys., 99, 1752
Alexander M. H., Li X., Liyanage R., Gordon R. J., 1998, Chem. Phys., 231, 331
Appenzeller I., Mundt R., 1989, A&AR, 1, 291
Asplund M., Grevesse N., Sauval A. J., Scott P., 2009, ARA&A, 47, 481
Badhan M. A., Wolf E. T., Kopparapu R. K., Arney G., Kempton E. M.-R., Deming D., Domagal-Goldman S. D., 2019, ApJ, 887, 34
Blake G. A., Keene J., Phillips T., 1985, ApJ, 295, 501
Brion C., Dyck M., Cooper G., 2005, J. Electron. Spectrosc. Relat. Phenom., 144-147, 127
Brown A., Balint-Kurti G. G., 2000, J. Chem. Phys., 113, 1870
Carnovale F., Tseng R., Brion C. E., 1981, J. Phys. B: At. Mol. Opt. Phys., 14, 4771
Cernicharo J. et al., 2010, A&A, 518, L136
Cheng B.-M., Chung C.-Y., Bahou M., Lee Y.-P., Lee L. C., 2002, J. Chem. Phys., 117, 4293
Clark V. H. J., Yurchenko S. N., 2021, Phys. Chem. Chem. Phys., 23, 11990
Colbert D. T., Miller W. H., 1992, J. Chem. Phys., 96, 1982
Curdt W., Brekke P., Feldman U., Wilhelm K., Dwivedi B. N., Schühle U., Lemaire P., 2001, A&A, 375, 591
de Beer E., Koenders B. G. P. K. M., de Lange C. A., 1990, J. Chem. Soc. Faraday Trans., 86, 2035
Draine B. T., 1978, ApJS, 36, 595
Engin S., Sisourat N., Carniato S., 2012, J. Chem. Phys., 137, 154304
Federman S., Cardell J. A., van Dishoeck E. F., Lambert D. L., Black J., 1995, ApJ, 445, 325
Fleury B., Gudipati M. S., Henderson B. L., Swain M., 2019, ApJ, 871, 158
France K. et al., 2016, ApJ, 820, 89
Gerin M., Neufeld D. A., Goicoechea J. R., 2016, ARA&A, 54, 181
Ginter D. S., Ginter M. L., 1981, J. Mol. Spectrosc., 90, 177
Givertz S. C., Balint-Kurti G. G., 1986, J. Chem. Soc. Faraday Trans., 82, 1231
Gordon I. E. et al., 2017, J. Quant. Spectrosc. Radiat. Transf., 203, 3
Grebenshchikov S. Y., 2016, J. CO2 Utilization, 15, 32
Green D. S., Bickel G. A., Wallace S. C., 1991, J. Mol. Spectrosc., 150, 303
Habets G. M. H. J., Heintze J. R. W., 1981, A&AS, 46, 193
Heays A. N., Bosman A. D., van Dishoeck E. F., 2017, A&A, 602, A105
Hill C., Yurchenko S. N., Tennyson J., 2013, Icarus, 226, 1673
Hitchcock A. P., Williams G. R. J., Brion C. E., Langhoff P. W., 1984, Chem. Phys., 88, 65
Husser T.-O., Wende-von Berg S., Dreizler S., Homeier D., Reiners A., Barman T., Hauschildt P. H., 2013, A&A, 553, A6
Lefebvre-Brion H., Liebermann H. P., Vázquez G. J., 2011, J. Chem. Phys., 134, 204104
Lewis N. K. et al., 2020, ApJ, 902, L19
Li G., Gordon I. E., Le Roy R. J., Hajigeorgiou P. G., Coxon J. A., Bernath P. F., Rothman L. S., 2013a, J. Quant. Spectrosc. Radiat. Transf., 121, 78
Li G., Gordon I. E., Hajigeorgiou P. G., Coxon J. A., Rothman L. S., 2013b, J. Quant. Spectrosc. Radiat. Transf., 130, 284
Li W.-B., Zhu L.-F., Yuan Z.-S., Liu X.-J., Xu K.-Z., 2006, J. Chem. Phys., 125, 154310
Liu Y., Sun Q., Liu Y., Xue J., Li R., Yan B., 2021, J. Quant. Spectrosc. Radiat. Transf., 271, 107737
Long J., Wang H., Kvaran Á., 2013, J. Chem. Phys., 138, 044308
López-Puertas M., Taylor F. W., 2001, Non-LTE Radiative Transfer in the Atmosphere. World Scientific, Singapore
Loyd R. O. P. et al., 2016, ApJ, 824, 102
Maas Z. G., Pilachowski C. A., 2018, AJ, 156, 2
Madhusudhan N., Agundez M., Moses J. I., Hu Y., 2016, Space Sci. Rev., 205, 285
Monje R., Lis D., Roueff E., Gerin M., De Luca M., Neufeld D., Godard B., Phillips T., 2013, ApJ, 767, 81
Monje R., Lord S., Falgarone E., Lis D., Neufeld D., Phillips T., Güsten R., 2014, ApJ, 785, 22
Natta A., 1993, ApJ, 412, 761
Nee J. B., Suto M., Lee L. C., 1985, J. Phys. B: At. Mol. Opt. Phys., 18, L293
Nee J. B., Suto M., Lee L. C., 1986, J. Chem. Phys., 85, 719
Neufeld D. A., Zmuidzinas J., Schilke P., Phillips T. G., 1997, ApJ, 488, L141
Neufeld D. A. et al., 2010, A&A, 518, L108
Noelle A. et al., 2020, J. Quant. Spectrosc. Radiat. Transf., 253, 107056
Pezzella M., Yurchenko S. N., Tennyson J., 2021, Phys. Chem. Chem. Phys., 23, 16390
Regan P., Langford S., Cook P., Orr-Ewing A., Ashfold M. R. et al., 1999, Phys. Chem. Chem. Phys., 1, 3247
Regan P. M., Ascenzi D., Brown A., Balint-Kurti G. G., Orr-Ewing A. J., 2000, J. Chem. Phys., 112, 10259
Schilke P., Phillips T., Wang N., 1995, ApJ, 441, 334
Schinke R., 1993, Photodissociation Dynamics. Cambridge Univ. Press, Cambridge
Sonnentrucker P. et al., 2010, A&A, 521, L12
Stibbe D. T., Tennyson J., 1998, New J. Phys, 1, 2
Teal D. J., Kempton E. M. R., Bastelberger S., Youngblood A., Arney G., 2022, ApJ, 927, 90
Teanby N. A., Showman A. P., Fletcher L. N., Irwin P. G. J., 2014, Planet Space Sci., 103, 250
Tennyson J., Yurchenko S. N., 2012, MNRAS, 425, 21
Tennyson J. et al., 2016, J. Mol. Spectrosc., 327, 73
Tennyson J. et al., 2020, J. Quant. Spectrosc. Radiat. Transf., 255, 107228
Tilford S., Ginter M., 1971, J. Mol. Spectrosc., 40, 568
Tilford S., Ginter M., Vanderslice J. T., 1970, J. Mol. Spectrosc., 33, 505
Uttenthaler S., Aringer B., Lebzelter T., Kaeufl H. U., Siebenmorgen R., Smette A., 2008, ApJ, 682, 509
Valiev R., Berezhnoy A., Gritsenko I., Merzlikin B., Cherepanov V., Kurten T., Wöhler C., 2020, A&A, 633, A39
van Dishoeck E. F., Black J. H., 1982, ApJ, 258, 533
van Dishoeck E. F., van Hemert M. C., Dalgarno A., 1982, J. Chem. Phys., 77, 3693
Venot O., Rocchetto M., Carl S., Hashim A. R., Decin L., 2016, ApJ, 830, 77

Vioque M., Oudmaijer R. D., Baines D., Mendigutía I., Pérez-Martínez R., 2018, A&A, 620, A128
Wakelam V. et al., 2012, ApJS, 199, 21
Wakelam V. et al., 2015, ApJS, 217, 20
Woods T. N. et al., 1996, J. Geophys. Res., 101, 9541
Youngblood A. et al., 2016, ApJ, 824, 101
Youngblood A. et al., 2017, ApJ, 843, 31
Yurchenko S. N., Lodi L., Tennyson J., Stolyarov A. V., 2016, Comput. Phys. Commun., 202, 262
Yurchenko S. N., Al-Refaie A. F., Tennyson J., 2018, A&A, 614, A131
Zhang D., 2008, Chem. Phys., 353, 87
Zmuidzinas J., Blake G., Carlstrom J., Keene J., Miller D., 1995, ApJ, 447, L125

SUPPORTING INFORMATION

Supplementary data are available at *MNRAS* online.

HCl.zip
HF.zip

Please note: Oxford University Press is not responsible for the content or functionality of any supporting materials supplied by the authors. Any queries (other than missing material) should be directed to the corresponding author for the article.

This paper has been typeset from a TEX/LATEX file prepared by the author.